Multi-Tissue Analysis Using Synchrotron Radiation Micro-CT Images

1st Michael Sieverts
Department of Mechanical Engineering
University of Utah
Salt Lake City, UT, 84112, USA
0000-0002-8115-0208

2ndNikita Rabbitt
Department of Mechanical Engineering
University of Utah
Salt Lake City, UT, 84112, USA
Nikita.Rabbitt@utah.edu

3rd Dilworth Y. Parkinson
Advanced Light Source
Lawrence Berkeley Laboratory
Berkeley, CA, 94720, USA
0000-0002-1817-0716

4th Douglas W. Sborov
Division of Hematology
Huntsman Cancer Institute
University of Utah
Salt Lake City, UT, 84112, USA
Douglas.Sborov@hci.utah.edu

5th Claire Acevedo
Department of Mechanical Engineering
Department of Biomedical Engineering
University of Utah
Salt Lake City, UT, 84112, USA
0000-0001-5425-3052

***Abstract*—When studying metabolic disease, it is essential to investigate the disease's effect on multiple tissues and identify any communication, or cross-talk, between organs, tissues, and cells. In bone marrow cancer, adipose tissue triggers inflammation and growth of malignant plasma cells within the bone marrow and results in localized bone loss. Synchrotron radiation microtomography imaging enables 3D quantitative analysis of bone and adipose tissues and provides high resolution to observe local changes in tissue microstructure. However, optimal imaging techniques differ for hard bone tissues (absorption imaging) and soft adipose tissues (phase-contrast imaging). Here we introduce a new technique that leverages image reconstruction and deep learning in combination with the high-resolution imaging capabilities of synchrotron radiation microtomography to gain insight into the marrow microenvironment of human bone samples. This approach allowed for successful tissue segmentation and analysis of human core samples. Using high-resolution images such as these could allow for a better understanding of early bone-related changes that may predict disease progression or bone fractures.**

***Index Terms*—bone, bone marrow, bone matrix, x-ray imaging, synchrotron radiation microtomography, image reconstruction, phase contrast, phase retrieval, semantic segmentation, deep learning, machine learning**

I. Introduction

In biomedical research, it is becoming clear that metabolic disorders (e.g., diabetes, cancer, heart diseases) and chronic inflammation trigger dysfunction in multiple organs and tissues of the body. Recent studies have shown that this inflammatory response is primarily due to the pro-inflammatory actions of adipose (fat) tissues [1]. In particular, adipocytes (i.e., fat cells composing adipose tissues) secrete inflammatory mediators [1], [2], which tend to boost the inflammation throughout the body. It is well established that in patients with obesity and type 2 diabetes, the increase in adipose tissue and high glucose levels promote inflammation in various organ systems, such as the cardiovascular system [3], the digestive system (gastrointestinal tract, pancreas, liver) [4]–[6], and the skeletal system [7]. This multi-tissue inflammation impairs the immune system and enhances the risk of disease and infection [8]. The 2016 IARC report shows that overweight and obese patients are at a high risk of developing cancer in the breast, colon, esophagus, stomach, bone marrow, and other sites [9]. In multiple myeloma specifically, studies have indicated that change in the bone marrow adipose tissue is a critical driver in the growth of malignant plasma cells and the formation of osteolytic bone lesions [10]. Recent research shows that in lesion regions, osteocyte cells interact with malignant plasma cells causing osteocyte death, which contributes to bone loss and osteolytic bone lesions [11], [12]. However, it is not yet known how adipose tissues contribute to the development and progression of multiple myeloma and whether they interact with other cells in this process. Finding an effective technique to investigate the multilevel interaction, or cross-talk, of tissues and cells would bring light to the complex pathogenesis of metabolic diseases [13]–[15].

A well-suited technique for multi-tissue analysis is synchrotron radiation micro-tomography (SRμCT) because it provides high-resolution visualization of tissues' 3D internal structure. SRμCT images can be used to measure tissue volumes and tissue densities. These measurements are valuable because they can correspond to tissue properties and remodeling. In the case of bone marrow cores, SRμCT can be used to image soft (adipose) tissue and hard (bone) tissue simultaneously, even with their different levels of x-ray absorption. However, simultaneously imaging these two tissues presents the critical challenge of selecting the most appropriate imaging technique. Absorption imaging is well suited for materials with high x-ray absorption, such as dense bone matrix, while phase imaging is more appropriate for materials with low absorption levels, such as soft adipose tissue. When imaging soft and hard tissues together within

NIOSH 5T42OH008414-16

a single sample, the differences in material properties make it difficult to select optimal imaging parameters, such as x-ray energy and propagation distance, as each material requires unique settings.

In this study, we combine image reconstruction and deep learning techniques to segment both adipose and bone tissue in high resolution SRμCT images of human bone marrow cores of patients than underwent a cancer diagnosis procedure. Using bone marrow samples from standard biopsies taken from the iliac crest, we aim to:

1) Validate SRμCT as an imaging modality to quantify properties of human bone marrow core biopsies, specifically, the bone microstructure and the adipose marrow tissue.
2) Characterize properties of bone and adipose tissue to observe evidence of inter-tissue interactions between these tissues (Fig. 1).

We hypothesize that malignant plasma cell development is correlated to increases in bone marrow adipocyte content and changes in osteocyte lacunar density and volume. This analysis can provide insight into the potential cross-talk between adipose tissue and osteocyte cells. This technique can be used in the future to explore the mechanisms of early bone-related cancer progression in the bone marrow of living cancer patients and prevent bone fractures.

II. Background

A. Structure of bone marrow

Bone marrow [16] is the soft, spongy tissue located in the core of most bones that produces the body's blood cells. Marrow fills the interstitial space within bones and consists of both adipose and bone tissue. In humans, there are two types of bone marrow: red marrow, which mainly consists of blood cells, and yellow marrow, which mainly consists of adipocytes. The bone marrow is the primary site where new blood cells are produced, explaining why bone marrow cancer is classified as a blood cancer [17].

Bone tissue is populated with osteocyte cells embedded within the bone matrix. These cells reside in the lacunar spaces, or voids within the bone. Osteocytes sense micromanage in the bone matrix and direct osteoblast and osteoclast cells to affected areas, which form and resorb the bone matrix to prevent fracture [18]–[20]. Defects in osteocyte-mediated remodeling can alter the mineral distribution within cortical bone and change microstructural features, which causes bone fragility [21].

B. Phase and absorption imaging using SRμCT

Computed tomography is a 3D imaging process where many 2D x-ray images of a rotating sample are captured over a range of angles (typically 180 degrees). These images are then used to reconstruct a 3D image of the sample computationally. Synchrotron microtomography SRμCT is x-ray tomography performed at a synchrotron facility, which allows imaging with high x-ray flux at micrometer-scale resolution. The SRμCT beamline used in this study, beamline 8.3.2 at the Advance Light Source, offers an energy range of 8 to 45 keV, a one-micron spatial resolution, and scan times of 10–100 seconds.

SRμCT is well suited to provide 3D structural information at the micrometer length scale inside skeletal tissues. Prior studies at beamline 8.3.2 have revealed how changes in bone microstructure (osteocyte lacunae, canals, and mineral density) associated with bone fragility diseases and treatments can specifically affect the bone's resistance to fracture [21].

Depending on the properties of the material being imaged with SRμCT, either phase imaging or absorption imaging can be used. A material's complex index of refraction determines the signal from absorption or phase imaging. Samples that absorb x-rays well, such as bone, are frequently imaged by measuring absorption contrast. In this case, x-ray energy is chosen for a given sample composition and size that considers both image contrast (which is improved at lower energies because samples are generally more absorbing at lower x-ray energies) and the transmission through the sample (a sufficient amount of x-rays must transmit through the sample to give enough signal for imaging).

Soft tissues absorb less x-rays, but the phase component of their index of refraction is much higher. While even at relatively low x-ray energies, these softer materials have low absorption contrast, the structures can be clearly seen with phase contrast. Phase contrast can be achieved with various experimental approaches. The most common approach at SRμCT beamlines is propagation-based phase contrast. In this approach, the detector is moved further away from the sample. This increased propagation distance affects the phase contrast signal in the image. For propagation-based phase contrast, a propagation distance is often set based on the sample's features of interest. The increased distance can often reveal additional features, but it can also degrade resolution and lead to streaking or other artifacts in the reconstructed data. Another aspect of phase contrast imaging is that it is common to perform phase retrieval on the collected projection images before performing tomographic reconstruction, which is meant to convert the collected data (which generally has contributions from both phase and absorption) into a map of the phase component of the index of refraction. Phase retrieval has been used to collect SRμCT images of other soft tissues, such as tendon and spinal cord [22], [23].

When simultaneously imaging soft and hard tissues, choosing an optimal x-ray energy and propagation distance becomes challenging because each material requires a different technique. Additionally, many of the phase retrieval methods for propagation-based phase imaging assume that the sample has a single material type, which does not hold for these multi-component biological samples. Having multiple materials present in a single sample makes it difficult to determine optimal imaging parameters.

The parameters used for both imaging (including energy and propagation distance) and reconstruction (phase retrieval and other tomographic reconstruction settings) can significantly impact the subsequent image analysis, especially when that analysis includes image segmentation followed by quantitative

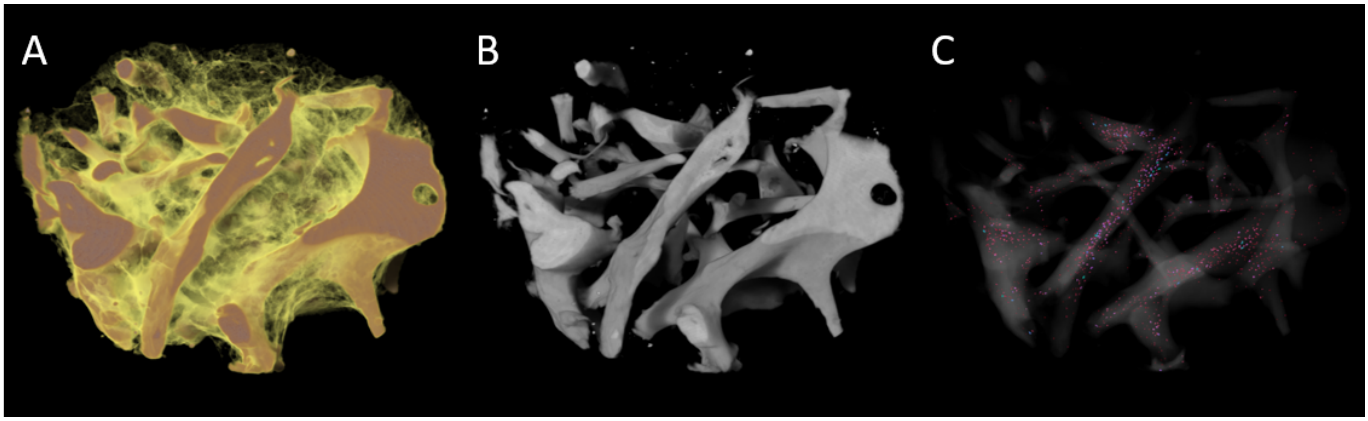

Fig. 1. Example 3D image of a bone core showing A) the bone and the fat (adipose) combined, B) the bone isolated, and C) the osteocyte lacunae.

analysis of the segmented structures. We compared different data collection and reconstruction parameters to identify a methodology that can segment structures from both soft and hard tissues at a high resolution in a single sample.

C. Segmentation of soft from hard tissues with different densities

Image segmentation is a necessary step in many image analysis workflows. The most straightforward approach to image segmentation is to set thresholds in the pixel intensity histogram where any pixels that fall within a given range in the histogram are assigned to a specific class. This approach is often applied after image filtering to reduce noise. This approach works well in SRμCT images of bone because it separates more absorbing tissue (bone) from the background. However, for soft tissue, the noise in the image causes many pixels in the background to be misclassified as soft tissue and vice versa. In recent years, segmentation using deep learning has become a common approach to overcome these types of challenges. Deep learning approaches use an initial ground truth segmentation to train a neural network, which can learn numerous characteristics beyond the pixel value intensity, such as texture and spacial relationships. These additional characteristics allow for more accurate segmentation. Once the network has been trained, it can be used to segment other similar images. A network architecture widely used for image segmentation in biomedical and material science applications is the U-net [24], [25].

The U-net is a fully convolutional neural network that encodes an image through a series of contracting layers and then decodes the encoding through a series of expanding layers to achieve the segmentation [24]. The U-net has successfully segmented biomedical images from many modalities, including magnetic resonance, computed tomography, and microscopy [25]. In addition to the U-net's success in biomedical imaging applications, the U-net has been used in material science applications [26], [27]. Recently, the U-net has been applied to segment SRμCT images of different tissues and materials [28]–[31]. Because of the U-net's well established success in image segmentation, it was selected as the network architecture for segmentation in this work.

III. Methods

A. Core samples

Patient samples were collected with the approval of the University of Utah Institutional Review Board (Protocols 45880, 89989), in accordance with the Declaration of Helsinki, during routine clinical care. Ten samples were obtained from ten different patients. Bone marrow core biopsies were collected from the posterior iliac crest and stored in 70% EtOH at 4°C. This technique is commonly used to diagnose bone marrow cancer [32]. This procedure involves using a hollow needle to acquire a red bone marrow sample from the ilium's crest under general or local anesthesia. Each cylindrical core has a diameter of 2 mm and a length near 5 mm.

This experiment was blinded. We did not have access to patient information or their potential disease stage. However, since these patients underwent this diagnostic procedure, they might be affected with bone marrow cancer with varying severity.

B. SRμCT imaging

The core samples were imaged at the tomography beamline (8.3.2) at the Advanced Light Source at Lawrence Berkeley National Lab. The samples were scanned with an energy of 20 keV. The images had a field of view of approximately 4mm with a 1.6 μm pixel size. Scans were collected with 1313 angles over 180 degrees, using a 50 micron LuAG:Ce scintillator from Crytur, a 4x lens in an optical system from Optique Peter, and a PCO.edge sCMOS camera.

C. Image reconstruction

The SRμCT scans were reconstructed using the gridrec algorithm implemented in the Python package Tomopy [33]. Phase retrieval was used in image reconstruction to assist in the segmentation of the two tissues in the scan. The single-step phase retrieval function in Tomopy was used during reconstruction [33], [34]. The level of phase retrieval was empirically adjusted to find a setting that yielded the best

overall segmentation of the two tissues present in the scan. As a proxy for varying all phase retrieval parameters, we scaled the level of phase retrieval by adjusting the parameter alphaReg (α) between values that would be optimal for bone and adipose tissue (0.1 to 0.0001). These reconstructed images were evaluated by analyzing the image histograms and observing the segmentation results of a double-Otsu threshold where the first Otsu was used to separate the dense bone tissue from the fat and the background. Then a second Otsu threshold was applied to the less dense region to segment the fat from the background [35].

D. Image segmentation

Image segmentation was performed using the Deep Learning Tools from the Dragonfly software, Version 2020.2 for Windows (Object Research Systems (ORS) Inc, Montreal, Canada, 2020). First, training data were produced using the Segmentation Wizard tool in Dragonfly. This tool allows the user to segment small regions of the image, which are then used to train machine learning models that aid in further segmentation. In this work, the models used to assist in segmenting training data included Random Forest, an Autoencoder, and a three-level U-Net [24]. The Segmentation Wizard allows for an iterative approach where the user segments a region of the scan, trains the machine learning models on the segmentation, uses the trained models to make predictions on a new region of the scan, and then corrects the models' segmentation predictions. This approach allows the user to quickly generate training data for segmentation. In this work, a total of 200 slices of training data were generated from 8 different scans (25 slices per scan). This training data was then used to train a model using Dragonfly's Deep Learning Tool.

A U-Net was trained to perform semantic segmentation using Dragonfly's Deep Learning Tool. The U-Net in this work had four encoding layers, a bottleneck layer, and four decoding layers. Each layer included two convolution steps and either a max-pool step during encoding or an up-sampling step during decoding. The first layer of convolutions had 32 filters, and each subsequent layer doubled the number of filters (32, 64, 128, 256, 512). During training, the training images were divided into square patches. A patch size of 256 pixels was chosen because it was large enough to provide the network with the necessary context to segment the image. The network was trained using Adadelta as the optimizer [36] with a learning rate of 1.0 and a decay rate (ρ) of 0.95. During training, a batch size of 32 patches was used. The loss function used to train the model was a custom function in Dragonfly called OrsDiceLoss. To monitor the network's performance during training, 20% of the training data was subset into a validation dataset. During training, the model was saved after each epoch when a reduction in the validation loss was observed. The network was set to train for 100 epochs with the condition that training would stop if ten epochs passed without an improvement in validation loss. The training was performed on the GPU using an Nvidia GeForce RTX 2080 TI.

A hold-out test dataset was used to evaluate the final model's performance. The performance was compared using the Dice Similarity Coefficient (DSC),

$$DSC = \frac{2|A \cap B|}{|A| + |B|},$$

where A represents the ground truth labels and B represents the segmentation. The values for the dice coefficient range from 0.0 to 1.0, where 1.0 indicates a perfect segmentation. The dice coefficient was computed for both the U-Net's segmentation and for the threshold-based segmentation.

E. Tissue analysis

Tissue analysis was performed for both the bone and adipose tissue using a combination of Dragonfly and Python (Anaconda Distribution). This software was used to determine tissue density and volume for the bone and adipose tissue present in the SRμCT scan. Density measurements from SRμCT scans can be used to describe material properties. For example, density measurements in bone can be used to estimate mineralization and stiffness of the tissue [37].

Tissue density was determined by creating a histogram of the segmented voxel intensities in the 32-bit scan with a bin width of 0.02. The peak position of the histogram was used as the value to represent the density of the tissue. Tissue grayscale intensities were converted to density measurements using the mass attenuation coefficient for either bone or adipose tissue. Tissue volume was calculated by counting the number of voxels assigned to a particular tissue and then converting the voxel count to a volume using pixel spacing.

In addition to tissue density and tissue volume, the bones' lacunae were analyzed. The lacunae were isolated using a grayscale intensity threshold and connected components (26-connected) on the SRμCT scans. Components with a volume either under 60 μm^3 or over 1000 μm^3 were excluded. The segmented lacunae were used to determine the mean lacunar volume and the lacunar density (the number of lacunae per bone volume) for each bone sample.

IV. Results & Discussion

A. Phase retrieval aids in separating the soft tissue from the background

The segmentation of adipose tissue from the background through thresholding was improved by applying a level of phase retrieval during reconstruction. These scans include three materials, air (background), adipose tissue, and bone. The histogram of the grayscale intensities would ideally have three peaks, one for each material. However, the pilot reconstruction without phase retrieval had a histogram with two peaks, one for dense bone tissue and one that included both adipose tissue and the background (Fig. 2 A). This overlap of grayscale intensities between background and adipose tissue limits the capability of threshold-based segmentation (Fig. 2 A). The image histogram changed with the different levels of phase retrieval. In the reconstruction with an α value of 0.01, most of the soft tissue and background fall into two distinct

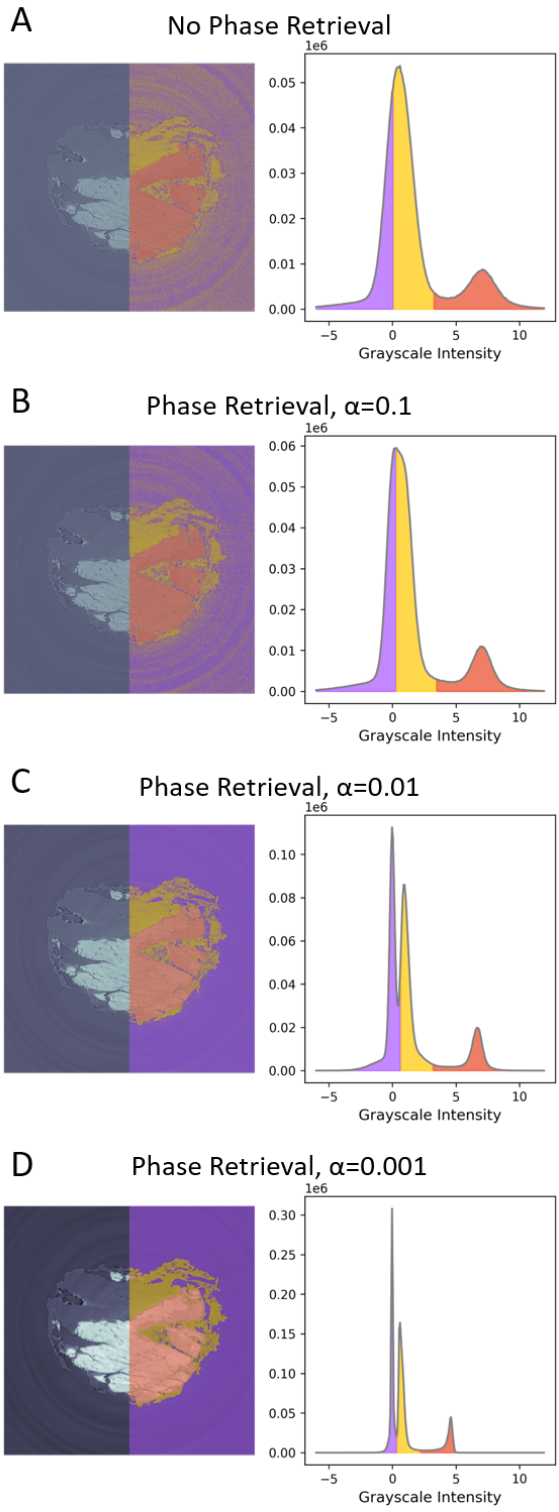

Fig. 2. Reconstruction results using different levels of phase retrieval. The left column contains examples of reconstructed images with with their double-Otsu segmentation. The right column contains the histograms that correspond to each image and to the image segmentation.

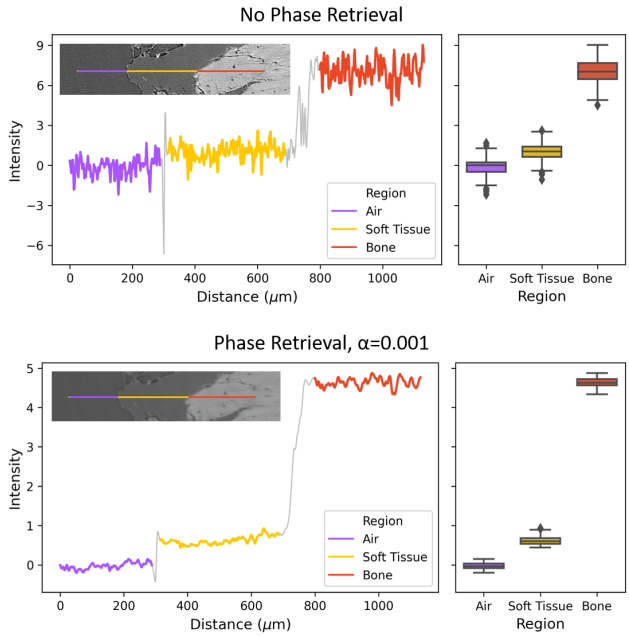

Fig. 3. Line profiles and box plots highlighting how phase retrieval affects the reconstructed images. The line profiles show how image intensities vary through different tissues. The box plots graph the distribution of intensity values in each tissue while ignoring the transition regions, which are shown on the line profile in gray. The top row shows results for no phase retrieval, and the bottom row shows results for phase retrieval with an α value of 0.001.

peaks in the histogram (Fig. 2 C). This distinction of soft tissue and background improved with smaller α values until a value of 0.0001, where image quality seemed to deteriorate due to the level of phase retrieval. Based on these results, all reconstructions for this study were performed using phase retrieval with an α value of 0.001.

In addition to using image histograms to observe the effects of phase retrieval, line profiles were created to highlight the effect of phase retrieval on the reconstructed images. Using the line profiles, we observed that phase retrieval increased the variance of grayscale intensities between tissues and decreased the variance of intensities within each tissue (Fig. 3). Increasing the relative variance of grayscale intensities between tissues helps illustrate the effectiveness of using phase retrieval to distinguish the soft adipose tissue from the background.

B. Deep learning segmentation successfully segments tissues

Deep learning segmentation was used to improve the segmentation results beyond the threshold technique. On a hold-out test set of data, the deep learning model achieved a dice coefficient of 0.994; on the same dataset, the threshold-based segmentation achieved 0.916 (Fig. 4). A dice coefficient for a perfect segmentation is 1.0, so a dice coefficient of 0.994 denotes a very successful segmentation. The bone and adipose tissue were successfully segmented using the U-net implemented in Dragonfly's Deep Learning Tool. The network trained for 44 epochs, at which point the validation loss had not improved in 10 epochs. The weights for the final model used in

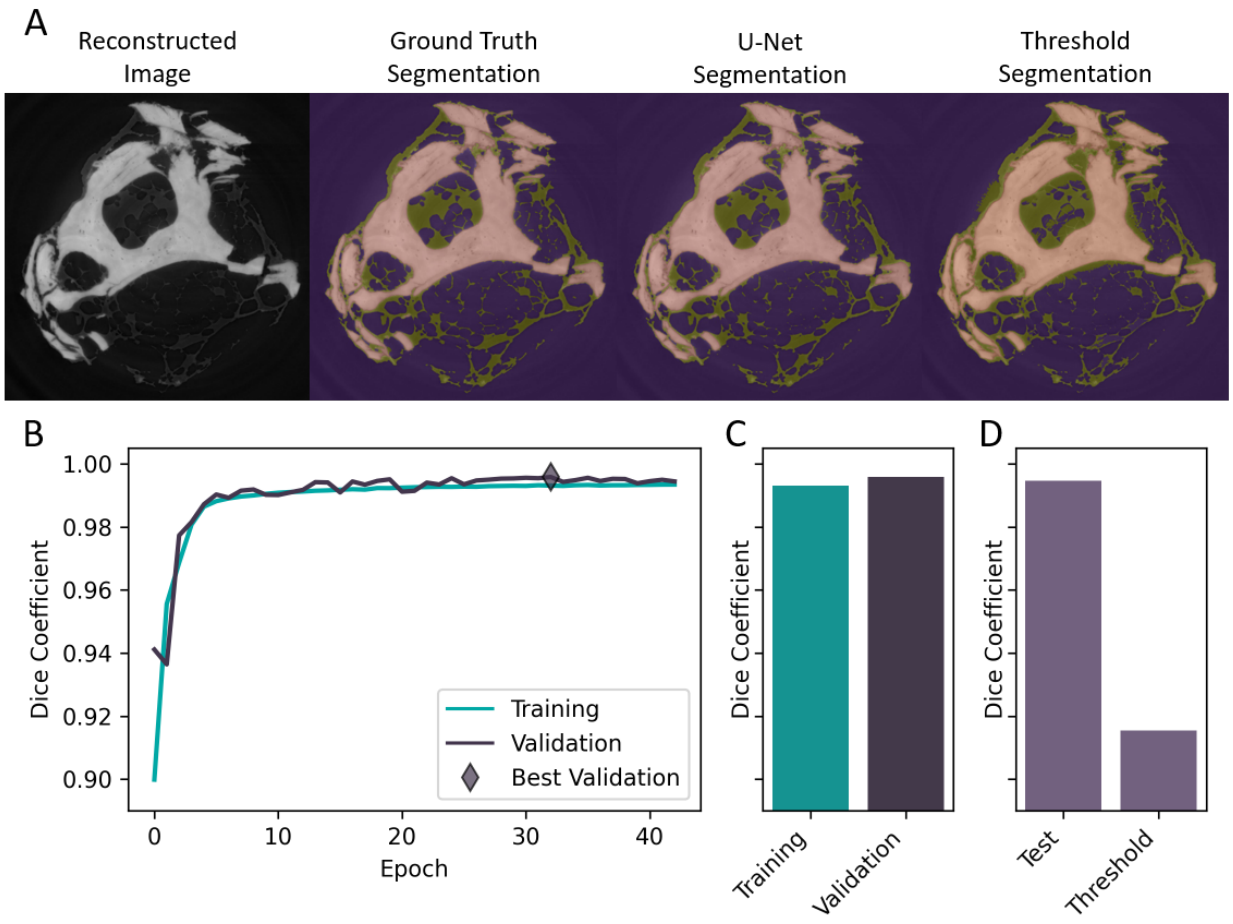

Fig. 4. Deep Learning segmentation results. A) Examples of the reconstructed image slice, the ground truth segmentation, the U-net segmentation, as well as the threshold-based segmentation. B) The line plot showing how the dice coefficient improved during training. C) The bar plots show the training and validation dice coefficients of the model at its best performing epoch (epoch 34), and D) the dice coefficients for the models performance on the test set and on the threshold-based segmentation approach.

this study were saved at epoch 34 when the lowest validation loss was recorded. The dice coefficients for the training and validation datasets using the final model were 0.993 and 0.995, respectively. The U-net's segmentation results were used to analyze the core samples further.

C. Tissue analysis metrics obtained from SRμCT images

We used the reconstruction and segmentation techniques presented in this work to measure properties of both bone and adipose tissue. Using the segmented images, we extracted tissue density and tissue volume measurements for each sample's bone and adipose tissue. The tissue density results for both tissues were represented as heat maps to visualize the variation in density distribution between samples (Fig. 5). Reviewing the density distribution for bone, we observed that two samples, sample 1 and sample 8, had particularly low densities. Due to these low densities, we inspected the images for those samples and observed that they had very little bone present in the scan, and it appears the bone was less dense than the other samples. The other samples all had densities around similar values. The high bone marrow adipose tissue and the low bone tissue density might be signs of an advanced stage of the disease [38]–[40]. The median bone density peak position was observed at 1.63 g/cm^3, and the median soft-tissue density was 1.32 g/cm^3. The peak positions representing our samples' bone mineral density were within the expected range for bone density, 0.7-2.2 g/cm^3 [41]. The peak positions representing our samples' adipose tissue density were slightly elevated compared to a recent study that found adipose tissue density to be approximately 0.9 g/cm^3 [42], [43], which is comparable to that of fat tissue (0.92 g/cm^3). The elevated adipose tissue density values in our samples could be explained by the regions in the sample where bone transitions into fat. In these transition regions, it appeared that some dense material was not dense enough to be classified as bone, so it would end up being included in the adipose category. However, since the same U-Net model segmented all of the scans, the classification of tissues is consistent between all samples. The peak positions of the tissue density distributions were recorded and used as a feature in further analysis.

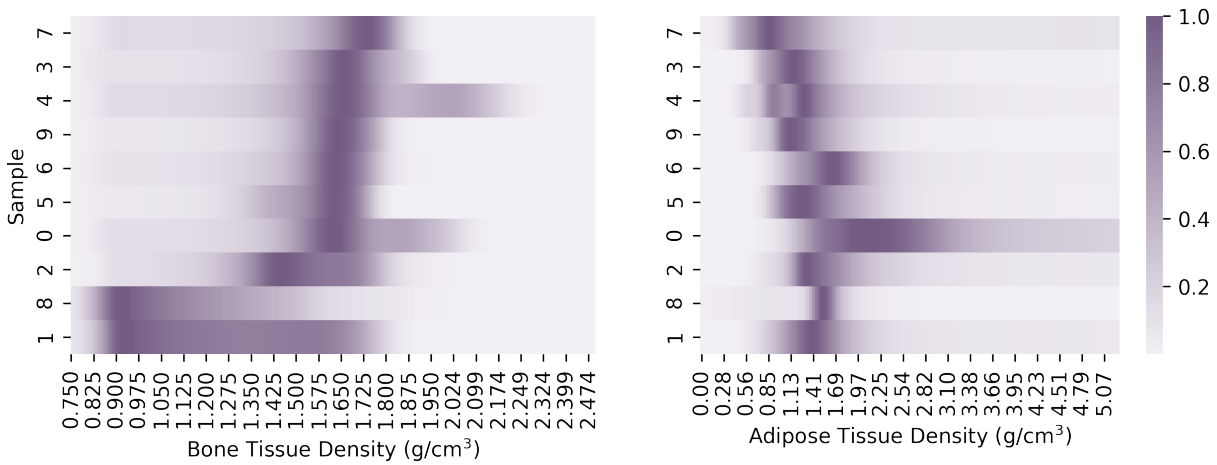

Fig. 5. Tissue density analysis for bone and soft tissue. The normalized histogram for each sample is represented as a row in the heat maps to compare similarities and differences between the density of the samples. The samples are sorted so the peak bone tissue density decreases from the top down. The heat map for bone's tissue mineral density is on the left and the heat map for soft tissue density is on the right.

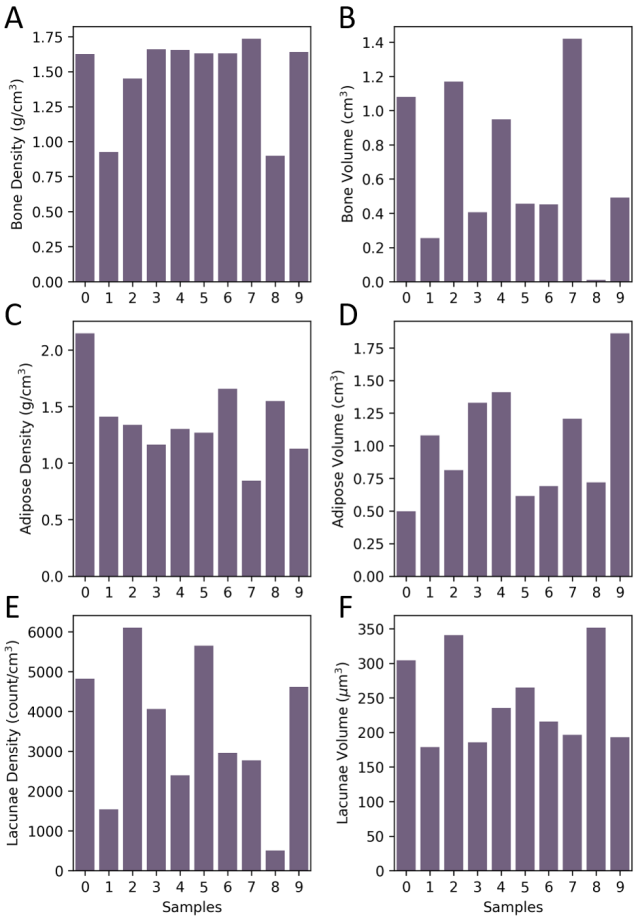

Fig. 6. Tissue analysis metrics for bone and adipose tissue. The top row shows metrics related to bone, A) bone tissue density and B) bone volume. The middle row shows metrics related to Adipose, C) Adipose tissue density and D) adipose volume. The third row shows metrics for the bone's lacunae, E) lacunae density (count of lacunae per bone volume) and F) mean lacunae volume.

Fig. 7. Correlation heat map showing the relationship between each variable. Correlations with a magnitude less than 0.4 were excluded from the heat map.

D. Metrics suggest possibility of inter-tissue relationships

Our results suggest a tentative relationship between adipose tissue and bone remodeling. Current literature discusses an inter-tissue relationship, or cross-talk, between adipose and bone tissue [11], [12], [44], [45]. To investigate this relationship, we used the Pearson correlation to compare the attributes of bone and adipose tissue that we recorded (Fig. 7). Two noteworthy correlations in this study were between adipose volume and lacunae volume (-0.63) and between adipose tissue density and lacunae volume (0.49). These correlations both relate measurements of adipose tissue to measurements of lacunar volume. Observing these correlations through SRμCT image analysis shows the potential to pair this technique with other tools to understand how these tissues influence each other. For example, changes in lacunar volume can be

associated with bone remodeling [46]. Recent publications have confirmed that bone marrow adipocytes impact bone remodeling through gene expression; however, there is still much to be learned about this relationship [47]–[49]. While the correlative relationships in this work are slight, they provide a pilot investigation into the relationship between bone and adipose tissue through SRμCT imaging. These correlations are limited by the number of samples in this study. A more in-depth study with larger sample sizes would need to be performed to make any strong claims about the relationships between these variables.

E. Method generalization

In this work, we develop a method for simultaneous SRμCT imaging of fat and hard tissues. This technique can be applied to explore the impact adipose tissue has on other tissues. Since elevated adipose tissue and glucose levels seem to promote inflammation in the body [1], [3], there could be interesting effects to explore. This technique could also be generalized and applied to study additional soft tissues that share an interface with bone, such as tendon, ligament, and cartilage [22], [50], [51]. For instance, the inflammatory response of the bone-cartilage interface causing osteoarthritis can be investigated with this SRμCT technique. Cross-talks and action-reaction between muscles and bones in musculoskeletal systems can also be a potential target for this technique.

F. Limitations

While the approach outlined here enables segmentation and analysis of the multiple tissues, there are limitations accompanying conclusions about the samples. One fundamental limitation is the lack of a healthy control group. A healthy control group and additional information about the samples affected by the disease would be required to understand how it impacts these tissues and their relationship. When analyzing correlations between the tissue measurements, a much larger sample size would be required to add confidence to the findings. Despite the lack of solid conclusions about the samples, the technique developed here effectively collected tissue measurements. This technique could be used in a study with improved sample groups to conclude relationships between the tissues.

V. Conclusion

This work achieved multi-tissue analysis of SRμCT images through our approach of phase retrieval during image reconstruction and the use of deep learning semantic segmentation. Once the images were processed using these techniques, we obtained volume and density metrics for both bone and soft tissue in the same scan. This study analyzed variables and relationships related to bone and soft tissue using samples from a single group. We confirmed that our measurements were feasible and identified suggested relationships between attributes of the two tissues: the adipose tissue volume and density seem to be inversely correlated to the osteocyte lacunar volume. This work helps establish an approach to multi-tissue analysis that can be used in future studies to identify changes in bone and soft tissue related to conditions or diseases, such as cancer.

Acknowledgment

This work was supported in part by NIOSH 5T42OH008414-16. The opinions and findings of the authors do not necessarily reflect the view and opinions of NIOSH.

The resources at beamline 8.3.2. of the Advanced Light Source are supported by the U.S. DOE Office of Science User Facility under contract no. DE-AC02-05CH11231.

The patient samples used in this work were provided by the Division of Hematology Biorepository at University of Utah, which is supported by the National Cancer Institute of the National Institutes of Health under Award Number P30CA042014. We would like to acknowledge the efforts of Anthony D. Pomicter and Justin A. Williams for this assistance with sample collection and processing. The content is solely the responsibility of the authors and does not necessarily represent the official views of the NIH. Additional funding came from the Huntsman Center of Excellence in Hematologic Malignancies and Hematology as well as the Hematologic Malignancies and Hematology Disease Center, both at Huntsman Cancer Institute, University of Utah.

References

[1] G. Daryabor, D. Kabelitz, and K. Kalantar, "An update on immune dysregulation in obesity-related insulin resistance," *Scandinavian journal of immunology*, vol. 89, no. 4, p. e12747, 2019.

[2] J. Ye, Z. Gao, J. Yin, and Q. He, "Hypoxia is a potential risk factor for chronic inflammation and adiponectin reduction in adipose tissue of ob/ob and dietary obese mice," *American Journal of Physiology-Endocrinology and Metabolism*, vol. 293, no. 4, pp. E1118–E1128, 2007.

[3] T. Almdal, H. Scharling, J. S. Jensen, and H. Vestergaard, "The independent effect of type 2 diabetes mellitus on ischemic heart disease, stroke, and death: a population-based study of 13 000 men and women with 20 years of follow-up," *Archives of internal medicine*, vol. 164, no. 13, pp. 1422–1426, 2004.

[4] A. Adeshirlarijaney and A. T. Gewirtz, "Considering gut microbiota in treatment of type 2 diabetes mellitus," *Gut microbes*, vol. 11, no. 3, pp. 253–264, 2020.

[5] A. E. Butler, J. Janson, S. Bonner-Weir, R. Ritzel, R. A. Rizza, and P. C. Butler, "β-cell deficit and increased β-cell apoptosis in humans with type 2 diabetes," *Diabetes*, vol. 52, no. 1, pp. 102–110, 2003.

[6] N. C. Leite, G. F. Salles, A. L. Araujo, C. A. Villela-Nogueira, and C. R. Cardoso, "Prevalence and associated factors of non-alcoholic fatty liver disease in patients with type-2 diabetes mellitus," *Liver international*, vol. 29, no. 1, pp. 113–119, 2009.

[7] C. Wu, G. Xu, S.-Y. A. Tsai, W. J. Freed, and C.-T. Lee, "Transcriptional profiles of type 2 diabetes in human skeletal muscle reveal insulin resistance, metabolic defects, apoptosis, and molecular signatures of immune activation in response to infections," *Biochemical and biophysical research communications*, vol. 482, no. 2, pp. 282–288, 2017.

[8] G. Daryabor, M. R. Atashzar, D. Kabelitz, S. Meri, and K. Kalantar, "The effects of type 2 diabetes mellitus on organ metabolism and the immune system," *Frontiers in immunology*, vol. 11, p. 1582, 2020.

[9] B. Lauby-Secretan, C. Scoccianti, D. Loomis, Y. Grosse, F. Bianchini, and K. Straif, "Body fatness and cancer—viewpoint of the iarc working group," *New England journal of medicine*, vol. 375, no. 8, pp. 794–798, 2016.

[10] E. V. Morris and C. M. Edwards, "Adipokines, adiposity, and bone marrow adipocytes: Dangerous accomplices in multiple myeloma," *Journal of Cellular Physiology*, vol. 233, no. 12, pp. 9159–9166, 2018.

[11] N. Giuliani, M. Ferretti, M. Bolzoni, P. Storti, M. Lazzaretti, B. Dalla Palma, S. Bonomini, E. Martella, L. Agnelli, A. Neri *et al.*, "Increased osteocyte death in multiple myeloma patients: role in myeloma-induced osteoclast formation," *Leukemia*, vol. 26, no. 6, pp. 1391–1401, 2012.

[12] C. Falank, H. Fairfield, and M. R. Reagan, "Signaling interplay between bone marrow adipose tissue and multiple myeloma cells," *Frontiers in endocrinology*, vol. 7, p. 67, 2016.

[13] L. Yang, L. Yang, X. Wang, H. Xing, H. Zhao, Y. Xing, F. Zhou, C. Wang, G. Song, and H. Ma, "Exploring the multi-tissue crosstalk relevant to insulin resistance through network-based analysis," *Frontiers in endocrinology*, vol. 12, 2021.

[14] G. Zhang, H. R. Byun, Z. Ying, M. Blencowe, Y. Zhao, J. Hong, L. Shu, K. C. Krishnan, F. Gomez-Pinilla, and X. Yang, "Differential metabolic and multi-tissue transcriptomic responses to fructose consumption among genetically diverse mice," *Biochimica et Biophysica Acta (BBA)-Molecular Basis of Disease*, vol. 1866, no. 1, p. 165569, 2020.

[15] P. Martins Conde, T. Pfau, M. Pires Pacheco, and T. Sauter, "A dynamic multi-tissue model to study human metabolism," *NPJ systems biology and applications*, vol. 7, no. 1, pp. 1–16, 2021.

[16] Y. Li, Y. Meng, and X. Yu, "The unique metabolic characteristics of bone marrow adipose tissue," *Frontiers in endocrinology*, vol. 10, p. 69, 2019.

[17] M. J. Devlin and C. J. Rosen, "The bone–fat interface: basic and clinical implications of marrow adiposity," *The Lancet Diabetes & Endocrinology*, vol. 3, no. 2, pp. 141–147, 2015.

[18] L. F. Bonewald, "The amazing osteocyte," *Journal of Bone and Mineral Research*, vol. 26, no. 2, pp. 229–238, 2011.

[19] ——, "Osteocytes as dynamic multifunctional cells," *Annals of the New York Academy of Sciences*, vol. 1116, pp. 281–290, 2007.

[20] N. S. Dole, C. M. Mazur, C. Acevedo, J. P. Lopez, D. A. Monteiro, T. W. Fowler, B. Gludovatz, F. Walsh, J. N. Regan, S. Messina, D. S. Evans, T. F. Lang, B. Zhang, R. O. Ritchie, K. S. Mohammad, and T. Alliston, "Osteocyte-Intrinsic TGF-β Signaling Regulates Bone Quality through Perilacunar/Canalicular Remodeling," *Cell Reports*, vol. 21, no. 9, pp. 2585–2596, 2017. [Online]. Available: https://doi.org/10.1016/j.celrep.2017.10.115

[21] Y. Obata, H. A. Bale, H. S. Barnard, D. Y. Parkinson, T. Alliston, and C. Acevedo, "Quantitative and qualitative bone imaging: A review of synchrotron radiation microtomography analysis in bone research," *Journal of the mechanical behavior of biomedical materials*, vol. 110, p. 103887, 2020.

[22] M. Pierantoni, I. Silva Barreto, M. Hammerman, L. Verhoeven, E. Törnquist, V. Novak, R. Mokso, P. Eliasson, and H. Isaksson, "A quality optimization approach to image achilles tendon microstructure by phase-contrast enhanced synchrotron micro-tomography," *Scientific reports*, vol. 11, no. 1, pp. 1–14, 2021.

[23] M. C. Strotton, A. J. Bodey, K. Wanelik, M. C. Darrow, E. Medina, C. Hobbs, C. Rau, and E. J. Bradbury, "Optimising complementary soft tissue synchrotron x-ray microtomography for reversibly-stained central nervous system samples," *Scientific reports*, vol. 8, no. 1, pp. 1–18, 2018.

[24] O. Ronneberger, P. Fischer, and T. Brox, "U-net: Convolutional networks for biomedical image segmentation," in *International Conference on Medical image computing and computer-assisted intervention*. Springer, 2015, pp. 234–241.

[25] N. Siddique, S. Paheding, C. P. Elkin, and V. Devabhaktuni, "U-net and its variants for medical image segmentation: A review of theory and applications," *Ieee Access*, vol. 9, pp. 82 031–82 057, 2021.

[26] K. Choudhary, B. DeCost, C. Chen, A. Jain, F. Tavazza, R. Cohn, C. W. Park, A. Choudhary, A. Agrawal, S. J. Billinge *et al.*, "Recent advances and applications of deep learning methods in materials science," *npj Computational Materials*, vol. 8, no. 1, pp. 1–26, 2022.

[27] S. M. Azimi, D. Britz, M. Engstler, M. Fritz, and F. Mücklich, "Advanced steel microstructural classification by deep learning methods," *Scientific reports*, vol. 8, no. 1, pp. 1–14, 2018.

[28] T. Strohmann, K. Bugelnig, E. Breitbarth, F. Wilde, T. Steffens, H. Germann, and G. Requena, "Semantic segmentation of synchrotron tomography of multiphase al-si alloys using a convolutional neural network with a pixel-wise weighted loss function," *Scientific reports*, vol. 9, no. 1, pp. 1–9, 2019.

[29] S. Ali, S. Mayo, A. K. Gostar, R. Tennakoon, A. Bab-Hadiashar, T. MCann, H. Tuhumury, and J. Favaro, "Automatic segmentation for synchrotron-based imaging of porous bread dough using deep learning approach," *Journal of Synchrotron Radiation*, vol. 28, no. 2, pp. 566–575, 2021.

[30] W. M. Tun, G. Poologasundarampillai, H. Bischof, G. Nye, O. King, M. Basham, Y. Tokudome, R. Lewis, E. Johnstone, P. Brownbill *et al.*, "A massively multi-scale approach to characterizing tissue architecture by synchrotron micro-ct applied to the human placenta," *Journal of the Royal Society Interface*, vol. 18, no. 179, p. 20210140, 2021.

[31] I. M. Baltruschat, H. Ćwieka, D. Krüger, B. Zeller-Plumhoff, F. Schlünzen, R. Willumeit-Römer, J. Moosmann, and P. Heuser, "Scaling the u-net: segmentation of biodegradable bone implants in high-resolution synchrotron radiation microtomograms," *Scientific reports*, vol. 11, no. 1, pp. 1–10, 2021.

[32] R. Trejo-Ayala, M. Luna-Pérez, M. Gutiérrez-Romero, J. Collazo-Jaloma, M. Cedillo-Pérez, and C. Ramos-Peñafiel, "Bone marrow aspiration and biopsy. technique and considerations," *Revista Médica Del Hospital General De México*, vol. 78, no. 4, pp. 196–201, 2015.

[33] D. Gürsoy, F. De Carlo, X. Xiao, and C. Jacobsen, "Tomopy: a framework for the analysis of synchrotron tomographic data," *Journal of synchrotron radiation*, vol. 21, no. 5, pp. 1188–1193, 2014.

[34] D. Paganin, S. C. Mayo, T. E. Gureyev, P. R. Miller, and S. W. Wilkins, "Simultaneous phase and amplitude extraction from a single defocused image of a homogeneous object," *Journal of microscopy*, vol. 206, no. 1, pp. 33–40, 2002.

[35] N. Otsu, "A threshold selection method from gray-level histograms," *IEEE transactions on systems, man, and cybernetics*, vol. 9, no. 1, pp. 62–66, 1979.

[36] M. D. Zeiler, "Adadelta: an adaptive learning rate method," *arXiv preprint arXiv:1212.5701*, 2012.

[37] S. Ma, O. Boughton, A. Karunaratne, A. Jin, J. Cobb, U. Hansen, and R. Abel, "Synchrotron imaging assessment of bone quality," *Clinical Reviews in Bone and Mineral Metabolism*, vol. 14, no. 3, pp. 150–160, 2016.

[38] P. K. Fazeli, M. C. Horowitz, O. A. MacDougald, E. L. Scheller, M. S. Rodeheffer, C. J. Rosen, and A. Klibanski, "Marrow fat and bone—new perspectives," *The Journal of Clinical Endocrinology & Metabolism*, vol. 98, no. 3, pp. 935–945, 2013.

[39] W. Shen, J. Chen, M. Punyanitya, S. Shapses, S. Heshka, and S. Heymsfield, "Mri-measured bone marrow adipose tissue is inversely related to dxa-measured bone mineral in caucasian women," *Osteoporosis international*, vol. 18, no. 5, pp. 641–647, 2007.

[40] T. A. Wren, S. A. Chung, F. J. Dorey, S. Bluml, G. B. Adams, and V. Gilsanz, "Bone marrow fat is inversely related to cortical bone in young and old subjects," *The Journal of Clinical Endocrinology & Metabolism*, vol. 96, no. 3, pp. 782–786, 2011.

[41] M. Mashiatulla, R. D. Ross, and D. R. Sumner, "Validation of cortical bone mineral density distribution using micro-computed tomography," *Bone*, vol. 99, pp. 53–61, 2017.

[42] T. Abe, R. S. Thiebaud, and J. P. Loenneke, "The mysterious values of adipose tissue density and fat content in infants: Mri-measured body composition studies," *Pediatric Research*, vol. 90, no. 5, pp. 963–965, 2021.

[43] U. A. Gurkan and O. Akkus, "The mechanical environment of bone marrow: a review," *Annals of biomedical engineering*, vol. 36, no. 12, pp. 1978–1991, 2008.

[44] S. Muruganandan, R. Govindarajan, and C. J. Sinal, "Bone marrow adipose tissue and skeletal health," *Current osteoporosis reports*, vol. 16, no. 4, pp. 434–442, 2018.

[45] Z. L. Sebo, E. Rendina-Ruedy, G. P. Ables, D. M. Lindskog, M. S. Rodeheffer, P. K. Fazeli, and M. C. Horowitz, "Bone marrow adiposity: basic and clinical implications," *Endocrine Reviews*, vol. 40, no. 5, pp. 1187–1206, 2019.

[46] G. Vahidi, C. Rux, V. D. Sherk, and C. M. Heveran, "Lacunar-canalicular bone remodeling: Impacts on bone quality and tools for assessment," *Bone*, vol. 143, p. 115663, 2021.

[47] M. Onji, N. Werschler, and J. Penninger, "A critical relationship between bone and fat: the role of bone marrow adipose-derived rankl in bone metabolism," *EMBO reports*, vol. 22, no. 7, p. e52986, 2021.

[48] Y. Hu, X. Li, X. Zhi, W. Cong, B. Huang, H. Chen, Y. Wang, Y. Li, L. Wang, C. Fang *et al.*, "Rankl from bone marrow adipose lineage cells promotes osteoclast formation and bone loss," *EMBO reports*, vol. 22, no. 7, p. e52481, 2021.

[49] W. Yu, L. Zhong, L. Yao, Y. Wei, T. Gui, Z. Li, H. Kim, N. Holdreith, X. Jiang, W. Tong *et al.*, "Bone marrow adipogenic lineage precursors

promote osteoclastogenesis in bone remodeling and pathologic bone loss," *The Journal of clinical investigation*, vol. 131, no. 2, 2021.

[50] M. K. Honkanen, A. E. Saukko, M. J. Turunen, R. Shaikh, M. Prakash, G. Lovric, A. Joukainen, H. Kröger, M. W. Grinstaff, and J. Töyräs, "Synchrotron microct reveals the potential of the dual contrast technique for quantitative assessment of human articular cartilage composition," *Journal of Orthopaedic Research®*, vol. 38, no. 3, pp. 563–573, 2020.

[51] K. H. Collins, D. J. Schwartz, K. L. Lenz, C. A. Harris, and F. Guilak, "Taxonomic changes in the gut microbiota are associated with cartilage damage independent of adiposity, high fat diet, and joint injury," *Scientific reports*, vol. 11, no. 1, pp. 1–7, 2021.